

# MnO(001) thin films on MgO(001) grown by reactive MBE using supersonic molecular beams

Andrew Pedersen, Junchen Liu, Fanxing Li, and H. Henry Lamb\*

Department of Chemical and Biomolecular Engineering, North Carolina State University, Raleigh, North Carolina 27695-7905

MnO(001) thin films were grown on commercial MgO(001) substrates at 520°C by reactive molecular beam epitaxy (MBE) using Mn vapor and O<sub>2</sub>-seeded supersonic molecular beams (SMB) both with and without radio-frequency (RF) plasma excitation. For comparison, MnO(001) films were grown by reactive MBE using O<sub>2</sub> from a leak valve. X-ray photoelectron spectroscopy (XPS) confirmed the Mn<sup>2+</sup> oxidation state and 10-15% excess oxygen near the growth surface. Reflection high-energy electron diffraction (RHEED) and X-ray diffraction (XRD) evidenced that the films were rock-salt cubic MnO with very strong (001) orientation. High-angle annular dark field (HAADF) scanning transmission electron microscopy (STEM) with energy-dispersive X-ray spectroscopy (EDS) demonstrated abrupt MnO/MgO interfaces and indicated [(001)<sub>MnO</sub>||(001)<sub>MgO</sub>] epitaxial growth. *Ex situ* atomic force microscopy (AFM) of films deposited without RF excitation revealed smooth growth surfaces. An SMB-grown MnO(001) film was converted to Mn<sub>3</sub>O<sub>4</sub> with strong (110) orientation by post-growth exposure to an RF-discharge (RFD) SMB source providing O atoms; the surface of the resultant film contained elongated pits aligned with the MgO<110> directions. In contrast, using the RFD-SMB source for growth resulted in MnO(001) films with elongated growth pits and square pyramidal hillocks aligned along the MgO<110> and <100> directions, respectively.

**Keywords:** MnO, Mn<sub>3</sub>O<sub>4</sub>, growth kinetics, XPS, AFM, HAADF-STEM, pipe diffusion

## I. INTRODUCTION

Manganese oxides comprise several stable compounds (i.e., MnO, Mn<sub>3</sub>O<sub>4</sub>, Mn<sub>2</sub>O<sub>3</sub>, and MnO<sub>2</sub>) with diverse chemical, electronic, and magnetic properties that find use in technological applications, such as ceramic pigments,<sup>1</sup> batteries,<sup>2,3</sup> semiconductor devices,<sup>4</sup> and catalysts.<sup>5</sup> Their multiple Mn oxidation states make them important redox catalysts in total and partial oxygen reactions<sup>6</sup>. Mn<sub>3</sub>O<sub>4</sub> and Mg<sub>6</sub>MnO<sub>8</sub> are two important redox catalysts that are used as oxygen donors (carriers) in chemical looping (CL) processes,<sup>7</sup> e.g., combustion and oxidative dehydrogenation (ODH).<sup>8</sup>

MBE provides precise (layer-by-layer) control of the composition of complex oxides enabling tailoring of surface redox sites.<sup>9</sup> The propensity of Mn to exist in multiple oxidation states poses challenges in synthesizing phase-pure thin films and requires careful control of growth conditions. Manganese monoxide (MnO) crystallizes in a rock-salt structure (*F* $\bar{m}$ 3*m* space group) with a lattice constant of 4.444 Å.<sup>10</sup> Growing MnO thin films can be challenging because the higher manganese oxides (e.g., Mn<sub>3</sub>O<sub>4</sub> and Mn<sub>2</sub>O<sub>3</sub>) are more thermodynamically stable.<sup>1</sup> Fritsch et al. conducted a detailed study on the thermodynamic properties on the manganese oxides.<sup>11</sup>

MnO(001) thin films have been grown by reactive evaporation of Mn on transition metal surfaces, including Ag(001), Au(111) and Pd(001).<sup>12-16</sup> Very low oxygen partial pressures (10<sup>-8</sup>-10<sup>-7</sup> torr) were used and typically the substrate was at room temperature (RT) during Mn deposition. Annealing in UHV or in a low-pressure O<sub>2</sub> ambient was used to adjust the stoichiometry and promote crystallization of the films.

Muller et al. (2002) grew epitaxial layers of MnO(001) on Ag(001) by depositing Mn at RT in an O<sub>2</sub> ambient. Stoichiometric MnO films were produced at O<sub>2</sub> partial pressures up to  $\sim 4 \times 10^{-7}$  torr, and the MnO(001) domains had good crystalline quality after post-growth annealing at  $\sim 400$  °C.<sup>15</sup> Similarly, Allegretti et al. employed reactive evaporation on Pd(001) substrates at 250 °C to grow MnO(001) films using an O<sub>2</sub> partial pressure of  $4 \times 10^{-7}$  torr; brief UHV annealing at 500-600 °C improved the surface structural order.<sup>12</sup> In contrast, Kundu et al. reexamined MnO(001)/Ag(001) growth and found that MnO was formed only for O<sub>2</sub> partial pressures  $< 1.5 \times 10^{-8}$  torr; higher O<sub>2</sub> partial pressures yielded Mn<sub>3</sub>O<sub>4</sub> (Hausmannite).<sup>16</sup> Bayer et al. reported that MnO(001) films on Pd(001) were oxidized to Mn<sub>3</sub>O<sub>4</sub> by annealing at 500 °C in  $1.5 \times 10^{-5}$  torr O<sub>2</sub>.<sup>13</sup> Möller et al. examined growth of manganese oxide films on Au(111) by reactive evaporation and found that Mn<sub>3</sub>O<sub>4</sub> was produced by annealing in  $\sim 5 \times 10^{-7}$  torr O<sub>2</sub> at 327 °C and MnO was formed by subsequent UHV annealing at 527 °C.<sup>14</sup>

To our knowledge, there has been no previous research on reactive MBE of MnO thin films on MgO. Previous studies focused either on higher Mn oxides grown by plasma-assisted MBE or MnO films deposited by physical vapor deposition (PVD) techniques, and phase purity and film quality were typical issues. MgO has a rock-salt crystal structure like MnO albeit with a smaller lattice constant (4.217 Å).<sup>17</sup> MgO(001) substrates are commercially available; however, the  $\sim 6\%$  lattice mismatch with MnO(001) makes epitaxial growth of monocrystalline films problematic. Guo et al. investigated growth of Mn<sub>3</sub>O<sub>4</sub> and MnO<sub>2</sub> on MgO(001) via plasma-assisted MBE.<sup>18-21</sup> Three manganese oxide phases and surface morphologies were identified: (1) Mn<sub>3</sub>O<sub>4</sub> with pyramidal hillocks aligned along the MgO [110] and [−110] directions; (2)  $\lambda$ -MnO<sub>2</sub>

characterized by flat surfaces decorated with pits aligned along these directions; and (3) a mixed oxide consisting of  $\text{Mn}_3\text{O}_4$  and  $\lambda\text{-MnO}_2$  having truncated pyramidal hillocks aligned along [110].<sup>22</sup> Xing et al. reported that post-growth exposure of  $\text{MnO}_2$  films to an RF oxygen plasma improved film crystallinity.<sup>22</sup> Utilizing an RF excitation to generate reactive species, however, could also result in film damage from ion bombardment (e.g.  $\text{O}_2^+$ ). Elongated growth pits were observed on the  $\lambda\text{-MnO}_2$  and  $\text{Mn}_3\text{O}_4$  films grown by plasma-assisted MBE<sup>19, 20</sup> notwithstanding that the RF plasma source employed was designed to provide atomic O for growth without significant ion bombardment of the substrate. Kashir et al. reported  $\text{MnO}$  films grown on  $\text{MgO}$  using pulsed laser deposition (PLD) and noted a substrate temperature-dependent variation in film composition and quality.<sup>23</sup> Films grown at 750 °C were a mixture of  $\text{MnO}$  and  $\text{Mn}_3\text{O}_4$  with high mosaicity, as evidenced by X-ray diffraction (XRD) rocking curves. Lowering the substrate temperature eliminated the  $\text{Mn}_3\text{O}_4$  phase and improved film smoothness and long-range order.

In this work, epitaxial  $\text{MnO}(001)$  films were grown on  $\text{MgO}(001)$  substrates by reactive MBE using Mn vapor and oxygen from three different sources: a UHV leak valve (LV), an  $\text{O}_2$ -seeded supersonic molecular beam (SMB), and an RF-discharge supersonic molecular beam (RFD-SMB). The UHV LV provides  $\text{O}_2$  molecules with low (thermal) average kinetic energy and a broad (Maxwell-Boltzmann) kinetic energy distribution. An  $\text{O}_2$ -seeded SMB delivers hyperthermal  $\text{O}_2$  molecules with a narrow energy distribution and an average kinetic energy that depends on the nozzle temperature and gas composition (for a fully expanded beam).<sup>24</sup> In an RFD-SMB, RF excitation heats the gas in the nozzle and produces a plasma containing electronically excited  $\text{O}_2$

molecules, O atoms and ions.<sup>25</sup> The average velocity of the seed species can be manipulated by the choice of diluent gas. In this work, no attempt was made to deflect ions emitted from the RFD-SMB source. The O<sub>2</sub>-seeded RFD-SMB also was used to oxidize MnO(001) films converting them (either partially or completely) to Mn<sub>3</sub>O<sub>4</sub>. The resultant films were characterized by reflection high-energy electron diffraction (RHEED), X-ray photoelectron spectroscopy (XPS), X-ray diffraction (XRD), atomic force microscopy (AFM), and scanning transmission electron microscopy (STEM) with energy dispersive spectroscopy (EDS).

## II. EXPERIMENTAL

### A. *Film Growth and Surface Analysis Tool*

Films were grown and characterized using a custom-built multi-chamber vacuum system comprising a UHV-compatible growth chamber, two UHV surface analysis chambers, a load lock, and high-vacuum transfer line.<sup>26</sup> A detailed schematic of the growth chamber and associated SMB line is provided in Fig. 1. The growth chamber is pumped by a Pfeiffer Hipace800 turbomolecular pump to a base pressure of 3 x 10<sup>-9</sup> torr. Substrates mounted on Mo holders are heated from the back side using a pyrolytic boron nitride (PBN) coated graphite heater powered by a Sorensen DC 40-75 power supply. The heated sample stage is positioned using a rotary/linear feedthrough, and the substrate temperature is monitored by a Type-K thermocouple and an infrared pyrometer (for temperatures >580 °C). Research-grade O<sub>2</sub> can be supplied via a UHV variable LV. A hot-lip Knudsen cell (SVT Associates) with a PBN crucible is installed with a 45° pitch angle relative to the substrate and powered by another Sorensen DC 40-75 power supply. RHEED patterns are measured *in situ* using a Fisons LEG 110 electron gun and phosphor

screen. The growth chamber is connected via a high-vacuum transfer line ( $\sim 10^{-8}$  torr) to a UHV surface analysis chamber equipped for XPS utilizing a PHI 3057 spectrometer with a PHI 80-865A spherical capacitor analyzer (SCA) and a PHI 04-548 Al/Mg dual anode X-ray source. The XPS chamber is pumped by a Perkin-Elmer TNBX ion pump to a base pressure of  $< 1 \times 10^{-10}$  torr.

The SMB nozzle assembly comprises a closed-end 6-mm PBN tube with a 140- $\mu\text{m}$  diameter laser-drilled orifice and a concentric RF helical resonator. The resonator is based on the designs of Pollard<sup>25</sup> and Wheeler, et al.<sup>27</sup> with 70 turns of 0.25-mm Ta wire wrapped around a 28-mm (outer diameter) BN mandrel. The RF tap is located at turn #20 from the grounded (upstream) end of the coil. Power is supplied via an ENI ACG 13.56-MHz RF generator and a MCS MTN-500 matching network. He and O<sub>2</sub> are metered to the nozzle via MKS mass flow controllers. When the RFD-SMB source was operated at 100 W using He and O<sub>2</sub> flow rates of 100 and 5.3 sccm, respectively, the resulting nozzle stagnation pressure was 180 torr. Alternatively, when operated for SMB growth without RF excitation, the He and O<sub>2</sub> flow rates were adjusted to 240 and 12.6 sccm, respectively, to achieve an equivalent stagnation pressure. The first differential pumping stage is evacuated by two Varian VHS-6 diffusion pumps; one of which is backed by a Leybold RUVAC WSU 251 Roots blower package and the other by an Alcatel 2033 mechanical pump. The beam passes through a conical stainless steel skimmer (Beam Dynamics) with a 1-mm aperture and enters the second stage that is evacuated by a Pfeiffer Hipace300 turbomolecular pump. The beam exits this stage through a 5-mm collimation aperture, enters the growth chamber, and impinges on 8-mm circular area on the substrate. During

operation the pressures in the first and second stages are  $\sim 1 \times 10^{-4}$  and  $\sim 4 \times 10^{-5}$  torr respectively, and the background pressure in the growth chamber is  $\sim 3 \times 10^{-7}$  torr.

The RFD-SMB source was characterized using a differentially pumped axial Pfeiffer Prisma quadrupole mass spectrometer located in the growth chamber. The relative intensities of the 16 and 32 m/z channels with the RF power turned on and off were compared to determine the O<sub>2</sub> dissociation fraction, and total fluxes were calibrated from the absolute intensities of these peaks.<sup>25</sup> Detailed calibration results are given in Supplemental Information. Plasma neutral temperatures (estimated as proportional to the square of the increase in stagnation pressure) were 830 to 930 °C<sup>28</sup>, and the highest dissociation fractions (and nozzle temperatures) were achieved (~6%) at the lowest O<sub>2</sub> flow rates (at constant He flow). Under conditions selected for growth (5% O<sub>2</sub>/He, 105 sccm, 100W RF input power, 0% reflected power, 180 torr stagnation pressure), the dissociation fraction was ~2%, and the plasma neutral temperature was 890 °C. The estimated O atom flux and average kinetic energy under these conditions were  $\sim 5 \times 10^{13}$  cm<sup>-2</sup> s<sup>-1</sup> and ~1.4 eV, respectively.

The hot-lip Knudsen cell was filled with Mn metal granules (99.98 %, VWR), and flux calibrations were made using a quartz crystal microbalance (KJ Lesker) in the substrate position. The K-cell temperature-flux data (Fig. S2, Supplemental Information) were fitted to a Clausius-Clapeyron relationship, and the estimated Mn heat of sublimation (258.1 kJ mol<sup>-1</sup>) agrees with the literature.<sup>29</sup> K-cell temperatures and the respective Mn fluxes employed for film growth are given in Table 1. The O<sub>2</sub> fluxes employed for growth using the LV, SMB and RF-SMB sources are also given in Table 1.

## B. Film Growth

Single-side-polished MgO(001) substrates (10 x 10 x 0.5 mm) were obtained from MSE Supplies. Each substrate was first sonicated in an isopropanol bath for 15 min. Subsequently, the unpolished side was coated with colloidal silver paste (PELCO), and the substrate was heated in a drying oven at 120 °C to dry and harden the lacquer creating a metallic layer for infrared absorption. The substrate was then mounted on a donut-shaped Mo holder using 0.2-mm molybdenum wire and inserted into the load lock. After *in situ* cleaning at 800 °C under  $5 \times 10^{-5}$  torr O<sub>2</sub> for 60 min, the MgO substrates gave streaky RHEED patterns and adventitious carbon contamination was <1 % by XPS. RHEED patterns (along the [100] and [110] azimuths) and an *ex situ* AFM image of an exemplary MgO(001) substrate are provided in Fig. S3 (Supplementary Information). The substrate is very smooth (RMS roughness = 0.068 nm for 5 x 5  $\mu\text{m}^2$  image); the diffuse streaks in the RHEED patterns along the [100] azimuth evidence small surface domains. Narrower streaks and multiple Kikuchi lines are found in the RHEED pattern along the [110] azimuth.

After *in situ* cleaning, the substrate temperature was lowered to 520 °C for growth. Film growth conditions (oxygen source, K-cell temperature, and growth time) are given in Table 2. To initiate the growth process, a gate valve was opened allowing the oxygen beam to impinge on the substrate. Alternatively, the variable LV was adjusted to obtain the desired O<sub>2</sub> partial pressure. Next, the Mn K-cell shutter was opened. When the growth time had elapsed, this sequence was reversed. Selected films were exposed after growth to either the SMB or RFD-SMB at 520 °C for 30 min in the absence of a Mn flux.

### C. **Film Characterization**

After *in situ* RHEED measurements, samples were transferred *in vacuo* to the XPS chamber. XPS scans were collected at a 45° takeoff angle with respect to the SCA axis using the Al X-ray anode operating at 300 W. Survey scans were conducted from 1400 to 20 eV binding energy (BE) with a 0.5-eV step size. Multiplex scans were conducted using a 23.5-eV pass energy and a 0.025-eV step size. XP spectra were analyzed using CasaXPS with corrections for surface charging made by adjusting the adventitious C 1s peak to 285 eV. *Ex situ* AFM images were obtained using an Asylum MFP-3D instrument. Tapping mode images were acquired using 300 kHz silicon tips at 256 x 256 pixels per frame with a 1 Hz raster rate. Images were taken at several scales from 20  $\mu$ m to 250 nm. Sets of images were taken at multiple surface locations to ensure images were representative. XRD was performed using a Rigaku Smartlab X-ray diffractometer with a Cu K $\alpha$  source. Scans covered a 2 $\theta$  range from 5° to 90° with a 0.02° step size. Substrates were oriented with the [100] direction aligned to the scanning axis of the instrument. Focused ion beam (FIB) pull-outs of selected films were made using a ThermoFisher Quanta 3D FEG scanning electron microscope. The FIB specimens were transferred to a ThermoFisher Titan 80-300 STEM to obtain cross-sectional images of the films. Images were taken operating at 200 kV using the HAADF camera along with EDS using 4 windowless Si drift detectors (Bruker). Bright-field TEM images and diffraction data were also obtained for selected specimens.

### III. RESULTS AND DISCUSSION

#### A. *Reactive MBE Growth Using Molecular Oxygen*

Manganese oxide films were grown on MgO(001) substrates at 520 °C by reactive MBE using a Mn K-cell temperature of 900 °C and two different O<sub>2</sub> partial pressures: 5 x 10<sup>-6</sup> and 5 x 10<sup>-5</sup> torr. These O<sub>2</sub> pressures are 1-2 orders of magnitude higher than reported for MnO growth on transition metals by reactive Mn evaporation at <350 °C (substrate temperature). The Mn 2p, Mn 3s, O 1s and Mg 1s XP spectra of a film grown under 5 x 10<sup>-6</sup> torr O<sub>2</sub> are shown in Fig. 2, and quantitative XPS results for the MBE films are provided in Table 2. Determining the Mn oxidation state using the Mn 2p<sub>3/2</sub> binding energy (BE) is not reliable because the values for MnO, Mn<sub>3</sub>O<sub>4</sub>, Mn<sub>2</sub>O<sub>3</sub>, and MnO<sub>2</sub> fall within an ~1 eV range, and the Mn 2p<sub>3/2</sub> peaks overlap for different species.<sup>30</sup> Fortunately, MnO is distinguished by the presence of high-BE satellites in the 2p region, such as those indicated in Fig. 2A.<sup>14, 16</sup> In addition, the multiplet splitting energy ( $\Delta$ ) of the Mn 3s peak can be used as a quantitative indicator of Mn oxidation state.<sup>15</sup> MnO, Mn<sub>3</sub>O<sub>4</sub>, Mn<sub>2</sub>O<sub>3</sub>, and MnO<sub>2</sub> exhibit multiplet splitting energies of approximately 6.1, 5.3, 5.4, and 4.4 eV, respectively;<sup>15, 30</sup> however, overlap of the Mn 3s and Mg 2s peaks necessitates deconvolution for MnO<sub>x</sub> thin films on MgO.<sup>15</sup> The observed multiplet splitting in Fig. 2B ( $\Delta = 6.13$  eV) is consistent with bulk MnO;<sup>27</sup> the area ratio of the parallel (low-energy) and anti-parallel (high-energy) Mn 3s peaks is ~1.7, whereas theory predicts a 1.4 (7/5) ratio. The O 1s peak at 530.0 eV (Fig. 2C) is symmetric with only a very small high-BE shoulder at 531.3 eV that can be tentatively assigned to surface OH groups from residual water vapor in the growth chamber. The O/Mn ratio indicates ~10% stoichiometric excess of oxygen in the near-surface region; MnO is known to

accommodate up to 5% excess oxygen in the bulk.<sup>31</sup> A very small Mg 1s peak is observed at  $\sim$ 1300 eV. The high-BE satellites in the Mn 2p XP spectrum of the MnO<sub>x</sub> film grown under  $5 \times 10^{-5}$  torr O<sub>2</sub> (not shown) are characteristic of MnO; however, the lower Mn 3s splitting and higher O/Mn ratio suggest the presence of higher oxidation state Mn species (*vide infra*).

RHEED patterns and *ex situ* AFM images of the MnO<sub>x</sub> films are shown in Fig. 3. For the MnO film grown at the lower O<sub>2</sub> pressure ( $5 \times 10^{-6}$  torr), the RHEED pattern along the [100] azimuth (Fig. 3A) shows a streaky pattern with diffuse Kikuchi lines. This RHEED pattern indicates that the film is aligned with the [100] substrate direction and rotating the sample through 90° produced an equivalent RHEED pattern evidencing square symmetry. The AFM images (Fig. 3C and 3E) reveal a growth surface with nanoscale ridges and grooves. The RMS roughness for the  $5 \times 5 \mu\text{m}^2$  image is 1.4 nm. The film grown using the higher O<sub>2</sub> partial pressure ( $5 \times 10^{-5}$  torr) displays a faint RHEED streak pattern with a lower background intensity (Fig. 3B). The AFM images (Fig. 3D and 3F) reveal a smoother film with an RMS roughness of 1.3 nm ( $5 \times 5 \mu\text{m}^2$  image size). The ridges and grooves in this film run diagonally (bottom left to top right) suggesting that the surface corrugation may arise from shadowing of the Mn beam.<sup>32</sup>

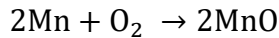
X-ray diffractograms of the MnO<sub>x</sub> films are shown in Fig. 4A. The film grown in a  $5 \times 10^{-6}$  torr O<sub>2</sub> ambient only contains peaks corresponding to the MnO ( $2\theta = 40.54^\circ$ ; 0.2223 nm) and MgO ( $2\theta = 42.89^\circ$ ; 0.2107 nm) (002) reflections; the measured *d* spacings match literature values within 0.5%.<sup>10, 17</sup> A wide (5-90°)  $2\theta$  scan (Fig. S5) shows no significant peaks assigned to other crystalline phases. The intense narrow MnO(002) peaks suggest low out-of-plane disorder. For the film grown in 5

$\times 10^{-5}$  torr O<sub>2</sub>, a third peak corresponding to the (004) reflection of Mn<sub>3</sub>O<sub>4</sub> ( $2\theta = 38.22^\circ$ ; 0.2353 nm) is also observed consistent with its higher near-surface O/Mn ratio (Table 2).<sup>33, 34</sup>

HAADF-STEM images and EDS maps of an FIB cross-section of the MnO film deposited at  $5 \times 10^{-6}$  torr are shown in Fig. 5. The film thickness (Fig. 5A) corresponds to a growth rate of 1.03 nm/min or 31% Mn incorporation. The lattice image (Fig. 5B) indicates that the (002) *d* spacings for MnO (0.228 nm in-plane, 0.223 out-of-plane) and MgO (0.218 nm in plane, 0.213 out-of-plane) are ~3% larger than expected;<sup>10, 17</sup> however, this is within the uncertainty of the STEM measurement. The film-substrate interface is abrupt with clear distinction between the two layers; however, the lattice near the interface is not well resolved. EDS maps (Fig. 5C-D) show no detectable interdiffusion of cations and uniform O atom concentrations in each phase.

A series of MnO films was grown using a 5% O<sub>2</sub>/He SMB and the Mn K-cell temperatures and growth times listed in Table 2. The 5% O<sub>2</sub>/He seeded beam provides a O<sub>2</sub> flux comparable to the low-pressure MBE experiment (Table 1); however, the O<sub>2</sub> molecules acquire hyperthermal kinetic energies (0.34 eV on average). Typically, the highly reflective films were clearly visible to the naked eye (Fig. S8, Supplemental Information). XPS measurements (Table 2) are consistent with stoichiometric MnO irrespective of Mn flux and growth time. X-ray diffractograms (Fig. 4B) of films grown for 60 min at different Mn fluxes contain only peaks corresponding to MnO(002) and MgO(002) consistent with [(001)<sub>MnO</sub>||(001)<sub>MgO</sub>] films. The films exhibit (002) *d* spacings that are 0.15-0.25% greater than in bulk MnO. This small out-of-plane lattice expansion decreases with increasing Mn flux and correlates linearly with the full-width

half maximum (FWHM) of the MnO(002) peak. Cross-sectional HAADF-STEM evidenced film thicknesses of 11.4 and 71.6 nm for films grown for 60 min using 853 and 900 °C K-cell temperatures, respectively. The corresponding growth rates are 0.19 and 1.2 nm min<sup>-1</sup>, and the Mn incorporation efficiencies are 14 and 34%, respectively. Plotting the growth rates of the MBE and SMBe films at constant Mn flux (900°C K-cell temperature) against the corresponding O<sub>2</sub> fluxes (Fig. 6A) yields a straight line through the origin indicating that the growth kinetics are first order in O<sub>2</sub>. In addition, plotting the MnO growth rates at constant O<sub>2</sub> flux (for the 5% O<sub>2</sub>/He SMB) against the square of the corresponding Mn flux (Fig. 6B) yields a straight line through the origin indicating that MnO growth kinetics are second order in Mn. These results are consistent with mass action kinetics based on the following stoichiometric equation:



The overall redox growth process likely involves multiple elementary steps, including Mn adsorption, O<sub>2</sub> dissociative chemisorption, O reduction to lattice oxygen (oxide ion, O<sup>2-</sup>) and Mn oxidation (to Mn<sup>2+</sup>).

RHEED and *ex situ* AFM images of a 45-nm MnO film grown using a 5% O<sub>2</sub>/He seeded SMB and a 900 °C Mn K-cell temperature are shown in Fig. 7. HAADF-STEM images are provided in Supplemental Information. The RHEED pattern along the [100] azimuth (Fig. 7A) is indicative of a smooth film aligned epitaxially with the MgO(001) substrate. Rotating the sample through 90° produced similar patterns consistent with 4-fold symmetry. AFM images (Fig. 7C and 7E) reveal a very smooth film without distinctive features (e.g., no ridges, valleys, or pits) and an RMS roughness of 0.39 nm (5 x 5 μm<sup>2</sup> image in Fig. 7E). XP spectra of the as-grown film contain Mn<sup>2+</sup> satellites in the

Mn 2p region (Fig. 8A), and the Mn 3s  $\Delta = 6.22$  eV (Fig. 8B) is consistent with stoichiometric MnO.<sup>15, 30</sup> The O 1s peak at 529.9 eV (Fig. 8C) is relatively narrow and symmetrical, with a ~2% hydroxyl concentration. The O/Mn ratio is 15% higher than expected for MnO but falls within the experimentally observed range (Table 2).

In a separate experiment, a MnO(001) film was grown under equivalent conditions and subsequently exposed to the 5% O<sub>2</sub>/He seeded SMB at 520 °C for 30 min. RHEED patterns and AFM images of the film after beam exposure are very similar to the as-grown film. Although the O/Mn ratio increased, the Mn 2p BE and the Mn 3s  $\Delta$  did not change significantly (Table 2). An apparent change in the area ratio of the parallel and anti-parallel Mn 3s peaks arises from overlap of the high-energy (anti-parallel) peak with the Mg 2s peak (Fig. 8B). The presence of Mg at the film surface after post-growth beam exposure probably accounts for the higher apparent O/Mn ratio (Fig. 8D). The MnO(002) XRD peak (Fig. 9A) shifted to higher  $2\theta$  values ( $2\theta = 40.884^\circ$ ; 0.2206 nm) indicating a 0.8% contraction of the out-of-plane lattice spacing relative to bulk MnO.

In another experiment, a MnO(001) film was grown under equivalent conditions and exposed to a 5% O<sub>2</sub>/He seeded RFD-SMB at 520°C for 30 min. The 100 W RFD-SMB source provides an O<sub>2</sub> flux of ~45% that provided by the 5% O<sub>2</sub>/He seeded SMB; however, ~2% of the O<sub>2</sub> is dissociated to O atoms. HAADF-STEM images (Supplemental Information) indicate that the resultant film is ~40 nm thick. The RHEED pattern along the [100] azimuth (Fig. 7B) is weak with concomitant development of faint half-order streaks. AFM images (Fig. 7D and 7F) reveal elongated pits along the [110] and [−110] directions, and there is an increase in surface roughness (0.8 nm RMS for the image in Fig. 6F). The characteristic Mn<sup>2+</sup> satellite peaks are no longer present in the Mn

2p XP spectrum after RFD-SMB exposure (Fig. 8A). In addition, the Mn 3s  $\Delta$  decreased, and the O/Mn ratio increased (Table 2) indicating that the film was converted to a higher oxide. The Mg 1s signal (Fig. 8D) also increased markedly because of diffusion of Mg<sup>2+</sup> ions through the film (*vide infra*). All of the XPS peaks are markedly broader relative to the as-grown film. The origin of this broadening is unclear, but it is may be related to differential charging associated with surface defects (e.g., the observed pits). XRD (Fig. 8A) reveals that the MnO(002) diffraction peak has been eliminated, and a new peak appears at  $2\theta = 44.68^\circ$  corresponding to Mn<sub>3</sub>O<sub>4</sub>(220) (0.2026 nm).

The above results indicate that the as-grown MnO(001)/MgO(001) film has been oxidized to Mn<sub>3</sub>O<sub>4</sub> by RFD-SMB exposure at 520 °C. The strong (110) orientation contrasts with the (001) orientation observed for Mn<sub>3</sub>O<sub>4</sub> films grown directly on MgO(001) by plasma-assisted MBE<sup>18</sup> and the mixed-phase film grown by reactive MBE at higher O<sub>2</sub> pressure (*vide supra*). Moreover, Bayer et al. reported that MnO(001) films on Pd(100) oxidized by annealing at 500 °C in  $1.5 \times 10^{-5}$  torr O<sub>2</sub> comprised highly (001)-oriented Mn<sub>3</sub>O<sub>4</sub>.<sup>13</sup> Guo et al. found that the Mn<sub>3</sub>O<sub>4</sub>(001) lattice vectors were aligned along the  $\langle 110 \rangle$  directions of the MgO(001) substrate. Similarly, Bayer et al. reported that MnO(001) films supported on Pd(100) were converted to (001)-oriented Mn<sub>3</sub>O<sub>4</sub> with the *a* and *b* lattice vectors along the  $\langle 110 \rangle$  directions. Their DFT calculations indicated that Mn<sub>3</sub>O<sub>4</sub>(001)/MnO(001) epitaxy was favorable despite the ~9% lattice mismatch because of the relatively low strain energy of Mn<sub>3</sub>O<sub>4</sub>(001) at twice the MnO(110) interplanar spacing. In our MnO(001)/MgO(001) films, however, the internal MnO(100) plane was converted to Mn<sub>3</sub>O<sub>4</sub> with the *c* axis parallel to the substrate resulting in (110) orientation.

The effects of post-growth RFD-SMB exposure also were investigated by electron microscopy using FIB cross sections. Fig. 10A shows a bright-field (BF) TEM image near the  $[(001)_{\text{MnO}}||(001)_{\text{MgO}}]$  interface of a 45-nm film grown by SMBE using a 900 °C K-cell temperature. The interface is indicated by the arrow, and lattice fringes of both rock-salt cubic phases are resolved. The interface shows dislocations occur every  $\sim$ 20 lattice spacings consistent with the 6% lattice mismatch between MnO and MgO. The MnO lattice is clearly visible in the higher magnification view shown in Fig. 9C; the MnO(200) spacing is  $\sim$ 3% larger than expected from crystallography. A wide field-of-view (FOV) EDS map (Fig. 10E) confirms that the interface is abrupt and flat, and the Mg concentration in the film is negligible. A BF-TEM image of a 40-nm  $\text{Mn}_3\text{O}_4$  film resulting from post-growth exposure of a SMB-grown MnO film to a 5%  $\text{O}_2/\text{He}$  RFD-SMB for 30 min is shown in Fig. 10B. The transition from MgO(001) to the Hausmannite  $\text{Mn}_3\text{O}_4$ (001) is apparent near the interface. Although both 2D lattices are square, the  $\text{Mn}_3\text{O}_4$ (001) lattice is rotated by 45° (in the plane) so that the lattice vectors align with the  $\langle 110 \rangle$  directions of the MgO lattice. This rotation makes the  $\text{Mn}_3\text{O}_4$ (110) plane parallel to the MgO(001) substrate. The  $\text{Mn}_3\text{O}_4$ (220)  $d$  spacing (Fig. 10D) agrees closely (within  $\sim$ 2%) with the value obtained by XRD. The wide FOV EDS map (Fig. 9F) shows a diffuse interface with significant Mg migration into the film.  $\text{Mg}^{2+}$  ion diffusion into (and through) the film is consistent with the Mg 1s XP spectrum (Fig. 8D). In addition, Mg plumes (P) are observed that roughly coincide with the surface pits seen by AFM. Dislocation pipe diffusion<sup>35, 36</sup> provides a possible Mg migration mechanism because the etch pits may be highlighting “pile-ups” of edge dislocations in the film.<sup>37</sup>

The physical removal of material during the etching process is likely the result of the volatilization of high oxide species<sup>38</sup>.

## **B. Reactive MBE Growth Using an RFD-SMB**

A second series of MnO films was grown at 520 °C using a 5% O<sub>2</sub>/He RFD-SMB and the Mn K-cell temperatures and growth times listed in Table 2. XP spectra of the film grown using the lowest Mn flux (853 °C K-cell temperature) show weak Mn 2p satellite features and a smaller Mn 3s  $\Delta$  = 6.05 eV. Moreover, the Mn 2p<sub>3/2</sub> BE and O/Mn ratio are higher than typical for MnO films (Table 2). The RHEED pattern (Fig. S9, Supplemental Information) is sharp with half-order streaks suggesting MnO surface reconstruction.<sup>39</sup> AFM images (Fig. S9, Supplemental Information) reveal a very smooth film with a roughness closely similar to the bare MgO substrate. XRD (Fig. 9B) indicates that the film is (001)-oriented MnO; however, the (002) diffraction peak is weak and broad, as expected for an ultrathin film. We suggest that competitive deposition and etching resulted in self-limiting growth because a thicker film grown under similar conditions by SMBE (*vide supra*).

RHEED patterns and AFM images of films deposited using the RFD-SMB source and a 900 °C K-cell temperature are shown in Fig. 10. The RHEED pattern of the film after 15 min growth (Fig. 11A) contains diffuse segmented streaks. *Ex situ* AFM shows a relatively smooth surface containing random growth pits. A film grown for 60 min under these conditions also exhibited diffuse segmented RHEED streaks (Fig. 11C) with faint Kikuchi lines. The corresponding AFM image (Fig. 11D) evidences a rougher surface (RMS = 0.61 nm) with a smaller number of deeper pits. XP spectra of this film evidence Mn 2p satellite peaks and Mn 3s multiplet splitting consistent with MnO. For films

grown using the RFD-SMB source, the Mn 2p<sub>3/2</sub> BE values are ~0.5 eV higher than for films grown using the SMB source (Table 1). Slight peak broadening was also detected. The X-ray diffractogram of this film (Fig. 9B) comprises only peaks corresponding to the (002) reflections of MnO and MgO. In contrast to the SMBE films that show a small lattice contraction, the MnO(002) peak position indicates that the film is fully relaxed with no detectable lattice contraction or expansion. The RHEED pattern (Fig. 11E) of a film grown for 120 min under these conditions is very diffuse but Kikuchi lines are visible. The corresponding AFM image shows ordered elongated pits and square pyramidal hillocks. The square pyramid bases are oriented along with the MgO [100] direction, and the pitch angle of the triangular facets is 0.85°. Similar pyramidal hillocks were observed on the Mn<sub>3</sub>O<sub>4</sub> phase by Guo et al.; however, the edges were aligned along the [110] and [1̄10] substrate directions.<sup>19-21</sup> The elongated pits exhibit preferred orientation along the MgO [110] and [1̄10] directions and resemble those seen for the SMB-grown film after exposure to the RFD-SMB (converting it to Mn<sub>3</sub>O<sub>4</sub>).

The film grown using a 900 °C K-cell temperature for 60 min was examined by HAADF-STEM using an FIB cross section (Fig. 12). The film thickness (33.2 nm, Fig. 12A) corresponds to a growth rate of 0.55 nm min<sup>-1</sup> or a 16% Mn atom incorporation efficiency. The inferred growth rate is approximately one-half that of the analogous SMBE film; however, the thickness falls on the best-fit linear correlation with O<sub>2</sub> flux found previously for the MBE and SMBE films (Fig. 6A). This observation suggests that the O atoms generated by the RFD-SMB source do not enhance the MnO growth rate significantly. Apparently, the high reactivity of Mn with O<sub>2</sub> dominates the MnO growth kinetics, and a small flux of O atoms is insufficient to increase the rate or result in growth

of higher Mn oxides (e.g.,  $\text{Mn}_3\text{O}_4$ ) under steady-state conditions. The EDS map (Fig. 12C) reveals an abrupt interface with no evidence of interdiffusion of cations. The HAADF-STEM image near the film-substrate interface (Fig. 12E) shows  $\text{MnO}(002)$  spacings are consistent the results for the SMBE and MBE films (~2% greater than bulk  $\text{MnO}$ ).

A  $\text{MnO}(001)$  film grown using the RFD-SMB source and a 900 °C K-cell temperature for 60 min was exposed to the RFD-SMB source for 30 min. The XP spectra show loss of Mn 2p satellite features, a small decrease in Mn 3s multiplet splitting and an increase in O/Mn ratio (Table 2) that are consistent with conversion of  $\text{MnO}$  to  $\text{Mn}_3\text{O}_4$ . This inference is corroborated by the broad  $\text{Mn}_3\text{O}_4(220)$  reflection that appears in the X-ray diffractogram (Fig. 8B). The  $\text{MnO}(002)$  reflection remains strong indicating that the film was not converted completely to  $\text{Mn}_3\text{O}_4$ ; however, the peak is shifted to higher  $2\theta$  indicating a lattice contraction of ~0.8%. HAADF-STEM images are shown in Fig. 12. A large pit or trench near the film surface and a large defect near the film-substrate interface are visible in Fig. 12B. The EDS map in Fig. 12D indicates that the subsurface defect is associated with Mg ion penetration into the film. A lattice image (Fig. 12F) taken near the interface shows that both  $\text{MnO}$  and  $\text{Mn}_3\text{O}_4$  domains are present. AFM images (Fig. 13) show clear evidence of etching and reveal distinct atomic steps. Trenches were carved into the film that are ~6 nm deep running along the [110] substrate direction. The smooth regions of the film (both on and between the plateaus) show atomic-scale steps. BF-TEM images (Fig. 13C-D) reveal more clearly the distribution of the two phases. No difference in the distribution of these two phases was notable between the trench and plateau regions. A wide FOV HAADF image (Fig. 13F) and the

corresponding EDS map (Fig. 13G) show Mg plumes coincide with the trench edges. These plumes, however, only penetrate about halfway through the film and do not reach the film surface. An XPS survey scan (not shown) evidenced less surface Mg than after RFD-SMB exposure of the SMB-grown film (Fig. 7) indicating less Mg diffusion through the film. We infer that the films grown using the RFD-SMB source contain fewer crystallographic defects (e.g., vacancies and edge dislocations) thus limiting oxidation to the near-surface region and inhibiting Mg diffusion.

Films grown using the RFD-SMB source and a 920 °C K-cell temperature for 15, 60 and 120 min also gave XPS results consistent with stoichiometric MnO (Table 2); however, the surface O/Mn ratios are 15-20% in excess of stoichiometric MnO, and the Mn 2p<sub>3/2</sub> BE values ( $641.5 \pm 0.1$  eV) are higher. RHEED patterns and AFM images of these films are provided in Supplemental Information (Fig. S10).

## IV. SUMMARY AND CONCLUSIONS

Epitaxial MnO(001) films were deposited on MgO(001) at 520 °C using Mn vapor and three different O<sub>2</sub> sources. We infer that rapid reaction of elemental Mn with O<sub>2</sub> dominates the growth kinetics because neither O<sub>2</sub> hyperthermal kinetic energy nor a small flux of O atoms increases the steady-state growth rate. Smooth (001)-oriented MnO films with a ridge-and-valley surface morphology were grown using the LV O<sub>2</sub> source at  $5 \times 10^{-6}$  torr, whereas films grown at  $5 \times 10^{-5}$  torr comprised both MnO and Mn<sub>3</sub>O<sub>4</sub>. Films grown using an O<sub>2</sub>-seeded SMB were highly oriented MnO(001) with a slight lattice expansion (0.15-0.27%) and very smooth surfaces. When a MnO(001) film was subsequently exposed to a RFD-SMB containing O atoms, it was converted to (110)-

oriented  $Mn_3O_4$  with elongated pits along the  $[110]$  and  $[\bar{1}\bar{1}0]$  substrate directions. In contrast, films grown using the RFD-SMB source were  $MnO(001)$  with elongated growth pits and square pyramidal hillocks aligned along the  $MgO\langle 110 \rangle$  and  $\langle 100 \rangle$  directions, respectively. We infer that the surface defects are caused by ion etching.

## ACKNOWLEDGMENTS

This research was sponsored by the National Science Foundation (NSF) (CBET-2116724). Data collection was performed in part at the Analytical Instrumentation Facility at North Carolina State University supported by funding from the NSF (ECCS-2025064). Special acknowledgements are also made for Roberto Garcia and Chris Winkler at AIF for their help with FIB Cross-sectioning and STEM images and for their assistance in data interpretation.

## REFERENCES

1. Vermeersch, E.; Pincé, P.; Jehlička, J.; Culka, A.; Rousaki, A.; Vandenabeele, P., Micro-Raman spectroscopy on pigments of painted pre-Islamic ceramics from the Kur River Basin (Fars Province, Iran): The case of manganese oxides identification. *J. Raman Spec.* **2022**, *53* (8), 1402-1414.
2. Lim, M. B.; Lambert, T. N.; Chalamala, B. R., Rechargeable alkaline zinc–manganese oxide batteries for grid storage: Mechanisms, challenges and developments. *Mat. Sci. and Eng.: R: Reports* **2021**, *143*, 100593.
3. Marsal, P.; River, R.; Kordesch, K.; Urry, L., Dry Cell." US Patent, 2960558. **1960**.
4. Ghosh, S. K., Diversity in the Family of Manganese Oxides at the Nanoscale: From Fundamentals to Applications. *ACS Omega* **2020**, *5* (40), 25493-25504.
5. Reidies, A. H., Manganese Compounds. *Ullmann's Encyc. of Ind. I Chem.* **2000**.
6. Ramesh, K.; Chen, L.; Chen, F.; Liu, Y.; Wang, Z.; Han, Y.-F., Re-investigating the CO oxidation mechanism over unsupported  $MnO$ ,  $Mn_2O_3$  and  $MnO_2$  catalysts. *Catalysis Today* **2008**, *131* (1), 477-482.
7. Arjmand, M.; Leion, H.; Mattisson, T.; Lyngfelt, A., Investigation of different manganese ores as oxygen carriers in chemical-looping combustion (CLC) for solid fuels. *App. Energy* **2014**, *113*, 1883-1894.

8. Neal, L. M.; Yusuf, S.; Sofranko, J. A.; Li, F., Oxidative Dehydrogenation of Ethane: A Chemical Looping Approach. *Energy Tech.* **2016**, *4* (10), 1200-1208.
9. Eom, C. J.; Kuo, D.-Y.; Adamo, C.; Moon, E. J.; May, S. J.; Crumlin, E. J.; Schlom, D. G.; Suntivich, J., Tailoring manganese oxide with atomic precision to increase surface site availability for oxygen reduction catalysis. *Nat. Comm.* **2018**, *9* (1), 4034.
10. Kuriyama, M.; Hosoya, S., X-ray Measurement of Scattering Factors of Manganese and Oxygen Atoms in Manganous Oxide. *J. Phys. Soc. Japan* **1962**, *17* (6), 1022-1029.
11. Fritsch, S.; Navrotsky, A., Thermodynamic Properties of Manganese Oxides. *J. Amer. Ceramic Soc.* **1996**, *79* (7), 1761-1768.
12. Allegretti, F.; Franchini, C.; Bayer, V.; Leitner, M.; Parteder, G.; Xu, B.; Fleming, A.; Ramsey, M. G.; Podloucky, R.; Surnev, S.; Netzer, F. P., Epitaxial stabilization of MnO(111) overlayers on a Pd(100) surface. *Phys. Rev. B* **2007**, *75* (22).
13. Bayer, V.; Podloucky, R.; Franchini, C.; Allegretti, F.; Xu, B.; Parteder, G.; Ramsey, M. G.; Surnev, S.; Netzer, F. P., Formation of Mn<sub>3</sub>O<sub>4</sub>(001) on MnO(001): Surface and interface structural stability *Phys. Rev. B* **2007**, *76* (16).
14. Möller, C.; Barreto, J.; Stavale, F.; Nilius, N., Manganese Oxide Thin Films on Au(111): Growth Competition between MnO and Mn<sub>3</sub>O<sub>4</sub>. *J. Phys. Chem. C* **2019**, *123* (13), 7665-7672.
15. Müller, F.; de Masi, R.; Reinicke, D.; Steiner, P.; Hüfner, S.; Stöwe, K., Epitaxial growth of MnO/Ag(001) films. *Surf. Sci.* **2002**, *520* (3), 158-172.
16. Kundu, A. K.; Menon, K. S. R., Growth and characterization of ultrathin epitaxial MnO film on Ag(001). *J. of Crys. Growth* **2016**, *446*, 85-91.
17. Sasaki, S.; Fujino, K.; Takéuchi, Y., X-ray determination of electron-density distributions in oxides, MgO, MnO, CoO, and NiO, and atomic scattering factors of their constituent atoms. *Proc. Japan Acad. Series B* **1979**, *55* (2), 43-48.
18. Guo, L. W.; Ko, H. J.; Makino, H.; Chen, Y. F.; Inaba, K.; Yao, T., Epitaxial growth of Mn<sub>3</sub>O<sub>4</sub> film on MgO(001) substrate by plasma-assisted molecular beam epitaxy (MBE). *J. of Crys. Growth* **1999**, *205* (4), 531-536.
19. Guo, L. W.; Makino, H.; Ko, H. J.; Chen, Y. F.; Hanada, T.; Peng, D. L.; Inaba, K.; Yao, T., Structural characteristic and magnetic properties of Mn oxide films grown by plasma-assisted MBE. *J. of Crys. Growth* **2001**, *227-228*, 955-959.
20. Guo, L. W.; Peng, D. L.; Makino, H.; Hanada, T.; Hong, S. K.; Sumiyama, K.; Yao, T.; Inaba, K., Structural characteristics and magnetic properties of  $\lambda$ -MnO<sub>2</sub> films grown by plasma-assisted molecular beam epitaxy. *J. of App. Phys.* **2001**, *90* (1), 351-354.
21. Guo, L. W.; Peng, D. L.; Makino, H.; Inaba, K.; Ko, H. J.; Sumiyama, K.; Yao, T., Structural and magnetic properties of Mn<sub>3</sub>O<sub>4</sub> films grown on MgO(001) substrates by plasma-assisted MBE. *J. Magnetism and Magnetic Mat.* **2000**, *213* (3), 321-325.
22. Xing, X. J.; Yu, Y. P.; Xu, L. M.; Wu, S. X.; Li, S. W., Magnetic Properties of  $\beta$ -MnO<sub>2</sub> Thin Films Grown by Plasma-Assisted Molecular Beam Epitaxy. *J. of Phys. Chem. C* **2008**, *112* (39), 15526-15531.
23. Kashir, A.; Jeong, H.-W.; Lee, G.-H.; Mikheenko, P.; Jeong, Y. H., Pulsed Laser Deposition of Rocksalt Magnetic Binary Oxides. *Thin Solid Films* **2019**, *692*, 137606.
24. Miller, D. R., Atomic and Molecular Beam Methods: Vol. 1. Scoles, G., Ed. 1998.
25. Pollard, J. E., Radio-frequency discharge source for beams of atomic nitrogen and oxygen. *Rev. Sci. Inst.* **1992**, *63* (2), 1771-1776.
26. Novotný, P.; Lamb, H. H., Nanostructured MoO<sub>x</sub> films deposited on c-plane sapphire. *J.Vac. Sci. & Tech. A* **2019**, *37* (5), 051504.

27. Wheeler, M. C.; Seets, D. C.; Mullins, C. B., Angular dependence of the dynamic displacement of O<sub>2</sub> from Pt(111) by atomic oxygen. *J. Chem. Phys.* **1997**, *107* (5), 1672-1675.
28. Sibener, S. J.; Buss, R. J.; Ng, C. Y.; Lee, Y. P., Development of a supersonic O(3PJ), O(1D2) atomic oxygen nozzle beam source. *Rev. Sci. Inst.* **1980**, *51*, 167-182.
29. Ehlert, T. C., A mass spectrometric study of the sublimation of manganese. *J. Inorg. and Nuc. Chem.* **1969**, *31* (9), 2705-2710.
30. Ilton, E. S.; Post, J. E.; Heaney, P. J.; Ling, F. T.; Kerisit, S. N., XPS determination of Mn oxidation states in Mn (hydr)oxides. *App. Surf. Sci.* **2016**, *366*, 475-485.
31. Smyth, D. M., Deviations from stoichiometry in MnO and FeO. *J. Phys. and Chem. of Solids* **1961**, *19* (1), 167-169.
32. Barranco, A.; Borras, A.; Gonzalez-Elipe, A. R.; Palmero, A., Perspectives on oblique angle deposition of thin films: From fundamentals to devices. *Progress in Mat. Sci.* **2016**, *76*, 59-153.
33. Aminoff, G., XXVIII. Über die Kristallstruktur von Hausmannit (MnMn<sub>2</sub>O<sub>4</sub>). *Zeitschrift für Kristallographie - Crystalline Materials* **1926**, *64*, 475 - 490.
34. Jarosch, D., Crystal structure refinement and reflectance measurements of hausmannite, Mn<sub>3</sub>O<sub>4</sub>. *Mineralogy and Petrology* **1987**, *37* (1), 15-23.
35. Lu, D.; Jiang, Q.; Ma, X.; Zhang, Q.; Fu, X.; Fan, L., Defect-Related Etch Pits on Crystals and Their Utilization. *Crystals* **2022**, *12* (11), 1549.
36. Szot, K.; Rodenbücher, C.; Bihlmayer, G.; Speier, W.; Ishikawa, R.; Shibata, N.; Ikuhara, Y. Influence of Dislocations in Transition Metal Oxides on Selected Physical and Chemical Properties *Crystals* [Online], 2018.
37. Amodeo, J.; Merkel, S.; Tromas, C.; Carrez, P.; Korte-Kerzel, S.; Cordier, P.; Chevalier, J., Dislocations and Plastic Deformation in MgO Crystals: A Review. *Crystals* **2018**, *8* (6), 240.
38. Eung-Jik Lee, E.-J. L.; Jin-Woong Kim, J.-W. K.; Won-Jong Lee, W.-J. L., Reactive Ion Etching Mechanism of RuO<sub>2</sub> Thin Films in Oxygen Plasma with the Addition of CF<sub>4</sub>, Cl<sub>2</sub>, and N<sub>2</sub>. *Japanese Journal of Applied Physics* **1998**, *37* (5R), 2634.
39. Henrich, V. E.; Cox, P. A., *The Surface Science of Metal Oxides*. Cambridge University Press: 1994.